Microstructural Characteristics and Mechanical Properties of Fiber Laser Welded-Brazed Mg Alloy-Stainless Steel Joint

A better understanding was sought of microstructural evolution at different temperatures and compositions during the laser welding-brazing of Mg alloys to stainless steel sheet

BY C. W. TAN, L. Q. LI, Y. B. CHEN, A. M. NASIRI, AND Y. ZHOU

ABSTRACT

AZ31B Mg alloy and 201 austenitic stainless steel were lap joined by a laser welding-brazing (LWB) process using a Mg-Al-Zn based welding wire. The influence of the process heat input on microstructure and mechanical properties of the dissimilar joint was investigated. Metallurgical bonding of immiscible Mg and Fe couple was achieved by the formation of continuous ultrathin reaction products at the fusion zone-steel interface, with a thickness varied from 0.5 to 3 μm, growing slowly with the increase of the heat input. The interfacial reaction products were identified as $Al_{19}Mn_4$ and Fe(Al) from the fusion zone to the steel, respectively. The tensile shear test indicated that joints produced at 5.4 kJ/cm heat input exhibited the highest mechanical resistance reaching 2472 N fracture load, representing a 75.4% joint efficiency relative to the Mg base metal. The failure occurred in the heat-affected zone (HAZ) of the Mg base metal, indicating a strong bond at the fusion zone-steel interface. The thermodynamic stability of the reaction products formed at the interface during the laser welding-brazing process was also evaluated in the temperature range of 400° to 1100°C using *FactSage* thermochemical software. The results were found to be in good agreement with the experimental results. The results contributed to a better understanding of microstructural evolution at different temperatures and compositions during the laser welding-brazing of Mg alloys to stainless steel sheet.

KEYWORDS

• Magnesium • Stainless Steel • Laser Welding-Brazing
• Microstructure • *FactSage* Thermochemical Software

Introduction

Magnesium and its alloys have been recently attracting much interest, prized for their excellent properties such as high specific strength, good castability, and good damping capacity (Refs. 1, 2). As the lightest metal used for structural components, magnesium offers great potential to reduce weight by replacing steel and aluminum, which is desirable for manufacturers striving to reduce vehicle weight and improve fuel efficiency. Currently, steels are the most common metallic materials used in the automotive industry. Therefore, a dissimilar combination of magnesium alloys and steel for fabrication of lightweight structural components would further lower the vehicle weight. Attaining reliable Mg-steel joints will, in return, expand the application of Mg alloys in the automotive industry.

Joining Mg to steel is, however, a huge challenge because of great differences in their melting point temperatures and immiscibility between Mg and Fe (Refs. 3–9). The melting points of Mg and Fe are 630° and 1535°C, respectively. In addition, the boiling point of Mg is 1091°C, lower than the melting point of Fe, so catastrophic vaporization of molten magnesium alloy will occur if they melt simultaneously (Ref. 3). The maximum solid solubility of Fe in Mg is only 0.00041 at.-%. Therefore, they do not react with each other or mix at ambient pressure (Ref. 10). As a result, metallurgical bonding of Mg and Fe will be possible provided an intermediate element is adopted to react with both immiscible Mg and Fe and achieve a metallurgical bond.

There are two main ways employed to achieve metallurgical bonding at the interface of Mg and steel, i.e., adding an interlayer element or compound in between the base metals (Refs. 4–9,

*C. W. TAN, L. Q. LI, and Y. B. CHEN are with State Key Laboratory of Advanced Welding and Joining, School of Materials Science and Engineering, Harbin Institute of Technology, Harbin, China. TAN is also with the Centre for Advanced Materials Joining, Department of Mechanical and Mechatronics Engineering, University of Waterloo, Waterloo N2L 3G1, Canada, along with A. M. NASIRI (*amnasiri@uwaterloo.ca*) and Y. ZHOU.*

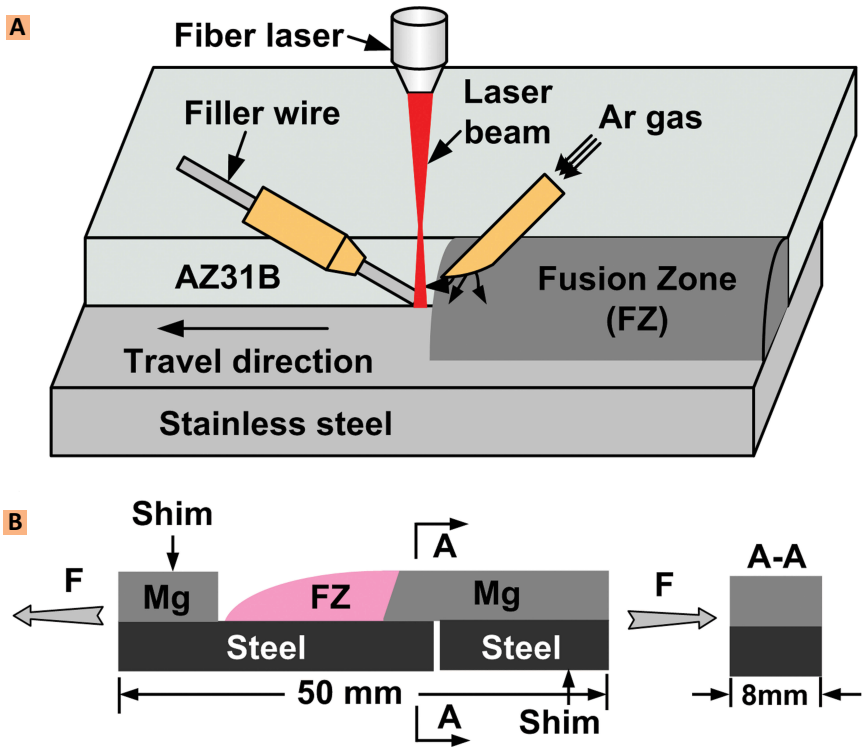

Fig. 1 — Schematic of the following: A — Laser welding-brazing process; B — 8-mm-wide tensile shear test specimen.

Table 2 — Chemical Composition of the Stainless Steel (wt-%)

Elements	C	Mn	Ni	Cr	Cu	V	Al	S	Si	P	Fe
Stainless Steel	≤0.15	10.7	0.53	14.7	1.21	0.108	0.36	≤0.03	≤0.75	≤0.06	Bal.

11–14), and using mutual diffusion of alloying elements from the base and filler metals (Refs. 15–19). Thin interlayers such as Cu, Ni, Sn, and Al have been applied between Mg and steel and heated to a high temperature to react with Mg from one side and with Fe from the other side, using different welding techniques (Refs. 4, 5, 7, 8, 12–14). A severe vaporization of upper Mg sheet was noticed during laser-gas tungsten arc hybrid welding (Refs. 4, 5, 7, 8), while formation of interfacial thick brittle reaction layers was reported during a liquid-phase bonding process (Refs. 12–14). The feasibility of joining Mg to steel through atomic interdiffusion at the interface was also investigated (Refs. 15–19). The friction stir welding (FSW) process has been reported to accelerate the diffusion of Al atoms from the Mg base metal to the steel with the combined actions of external force and strong stirring (Ref. 19). The interfacial reaction between Al and Fe resulted in the formation of a Fe-Al intermetallic compound (IMC) reaction product at the steel-Mg interface and hence a metallurgical bond was formed (Refs. 18, 19). However, a fresh and oxide-free steel surface was required, which was considered as a serious limitation of this process in sample preparation (Ref. 17).

The laser welding-brazing (LWB) process has been widely used in the automotive industry due to its unique performance such as high welding speed, low base metal deformation, and precise control of the laser beam energy (Refs. 20–24). It shows great advantages over FSW and conventional fusion welding due to its high flexibility and adaptability for practical applications. Miao et al. (Refs. 25, 26) used a laser brazing process to join Mg to steel without welding wire. In this process, part of the Mg base metal was melted to braze the steel. Crack and porosity formation

Table 1 — Chemical Composition of the AZ31B Mg Alloy and Filler Metal (wt-%)

Elements	Al	Zn	Mn	Fe	Si	Mg
AZ31B	2.92	1.09	0.3	0.005	0.1	Bal.
Filler metal	3.25	1.25	0.24	0.005	0.007	Bal.

were reported at the interface due to severe evaporation and oxidation of Mg as well as immiscibility between Mg and steel (Refs. 25, 26). Afterward, Nasiri et al. (Refs. 11, 27) performed the same process but added interlayers including Al-12Si and Ni. Using an Al-12Si coating layer resulted in formation of nonuniform, thick θ-Fe(Al,Si)$_3$ along the steel-fusion zone interface (Ref. 27). The tensile-shear strength of the 5-mm-wide laser brazed specimen reached 767±138 N (Ref. 27). In the case of the Ni interlayer, despite formation of α-Mg + Mg$_2$Ni eutectic phases and AlNi intermetallic compound in the fusion zone, formation of Fe(Ni) solid solution on the steel surface was reported as the key for metallurgical bonding of steel to Mg alloy (Ref. 11). The joint strength was reported to be 1506.3±24.5 N, which was 153% higher than that of the laser brazed, Al-coated steel-Mg alloy joint (Ref. 11). In our previous studies, a laser welding-brazing process using a welding wire was developed for joining Mg alloy to steel (Refs. 28–31). Stainless steel was found to promote the metallurgical bonding with Mg alloy (Ref. 29). However, the interfacial microstructure and bonding mechanism were not fully understood. Therefore, the purpose of this study was to further investigate the interfacial microstructure of laser welded-brazed Mg-steel dissimilar joints. Furthermore, to provide better understanding of the phases that might form at the interface of Mg alloy-stainless steel during the laser welding-brazing process, a thermochemical analysis using *FactSage* thermochemical software was conducted.

Experimental Procedures

Materials

AZ31B-H24 Mg alloy and 201 stainless steel sheets both with a thickness of 1.5 mm were selected as

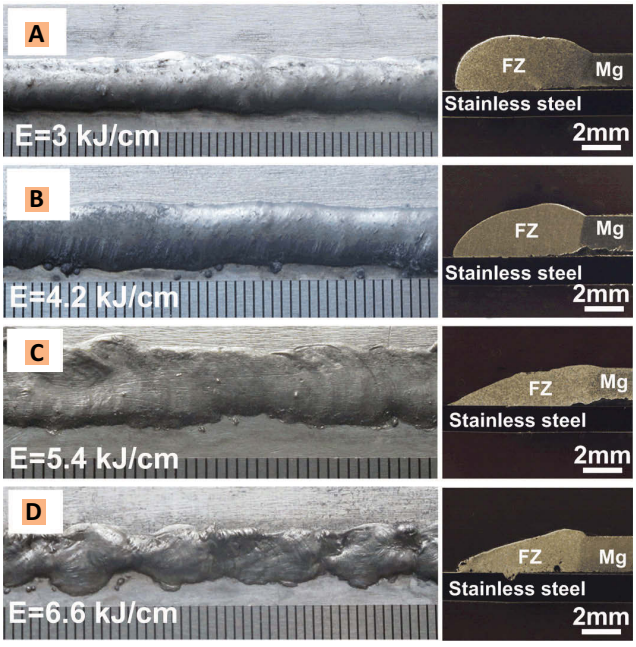

Fig. 2 — Laser brazed AZ31B Mg-steel made at different heat inputs: A — 3 kJ/cm; B — 4.2 kJ/cm; C — 5.4 kJ/cm; D — 6.6 kJ/cm.

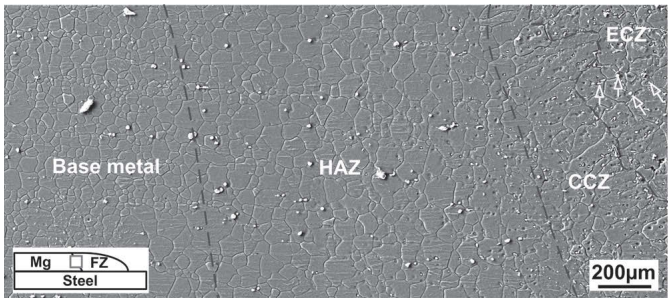

Fig. 3 — Photomicrograph of the fusion zone of the Mg side (Mg-FZ interface).

the base metals. A 2-mm-diameter Mg-Al-Zn-based alloy was used as the welding wire. The chemical compositions of the base metals and filler metal are listed in Tables 1 and 2, respectively. Flux QJ201 in powder form was used in the experiment with a chemical composition of 50 wt-% KCl, 32 wt-% LiCl, 10 wt-% NaF, and 8 wt-% $ZnCl_2$. The melting point of the flux was in the range of 460°–620°C. The sheets were cut into rectangular strips 30 mm wide and 100 mm long. Prior to welding, the surfaces of the Mg alloy sheets were cleaned with abrasive paper to remove surface oxides and the steel was ultrasonically cleaned in acetone to remove grease and other contaminants from the surfaces.

Laser Welding-Brazing Process

A fiber laser system with a maximum power of 10 kW (IPG YLR-10000) and a KUKA six-axis robot were used in this work. The laser beam had a wavelength of 1070 nm and a beam parameter product of 7.2 mm mrad. It was transmitted by a 200-μm core-diameter fiber and focused by a 200-mm lens to obtain a spot size of 0.2 mm.

The schematic of the LWB process is illustrated in Fig. 1A. The LWB experiments were carried out in a lap joint configuration, with the magnesium sheet clamped on the steel sheet. The laser beam was irradiated on the edge of the AZ31B Mg alloy vertically. Welding wire was fed in front of the laser beam. Argon shielding gas was provided to prevent oxidation. The angle of the welding wire and the workpiece were adjusted for smooth wire feeding. To completely irradiate the filler metal and promote brazing between molten filler metal and stainless steel, the laser beam was defocused.

Process Parameters

The main variables in the present work determining thermal gradient distribution and bead profile primarily included laser power, travel speed, and wire feed speed. Before the experiment, preliminary trials were carried out to obtain visually acceptable joints. The process parameters used in the experiment are listed in Table 3. The constant parameters during the LWB process were defocusing distance of positive 10 mm from the steel surface, 0.5-mm beam offset to the steel side, shielding gas flow rate of 20 L/min, and the angle of 30 deg between the welding wire and the steel.

Analysis Methods

After the LWB process, welded-brazed specimens were cut perpendicular to the travel direction. Standard grinding and polishing sample preparation procedures were then applied. The appearances and cross sections of the joints were observed using an optical microscope (OM). The microstructures and fracture surfaces were analyzed using a scanning electron microscope (SEM) equipped with an energy-dispersive X-ray spectrometer (EDS). A Tecnai-G^2 F30 transmission electron microscope (TEM) at a nominal voltage of 300 kV was used to characterize the microstructure in detail. Z-contrast images were acquired using a high-angle annular dark field (HAADF) detector in scanning transmission electron microscopy (STEM) mode. Phase identification was investigated by selected-area electron diffraction pattern (SADP) analysis. The specimens for tensile testing were cut 50 mm long and 8 mm wide, as shown in Fig. 1B, and subjected to a tensile shear test with a cross-head speed of 0.5 mm/min. Shims were clamped to each end of the specimens to ensure shear loads in the lap joint while minimizing bending or torque of the specimens.

Thermodynamic Analysis Procedure

In the study, the *FactSage* thermochemical software and databases were used to predict the phase formation and thermodynamic properties of the phases during LWB of AZ31B Mg-stainless steel multielement alloy system. It provided a more accurate way to predict phase formation in a complex multielement alloy system than just referring to the binary or ternary phase diagrams of the constituent elements. The thermochemical analysis was evalu-

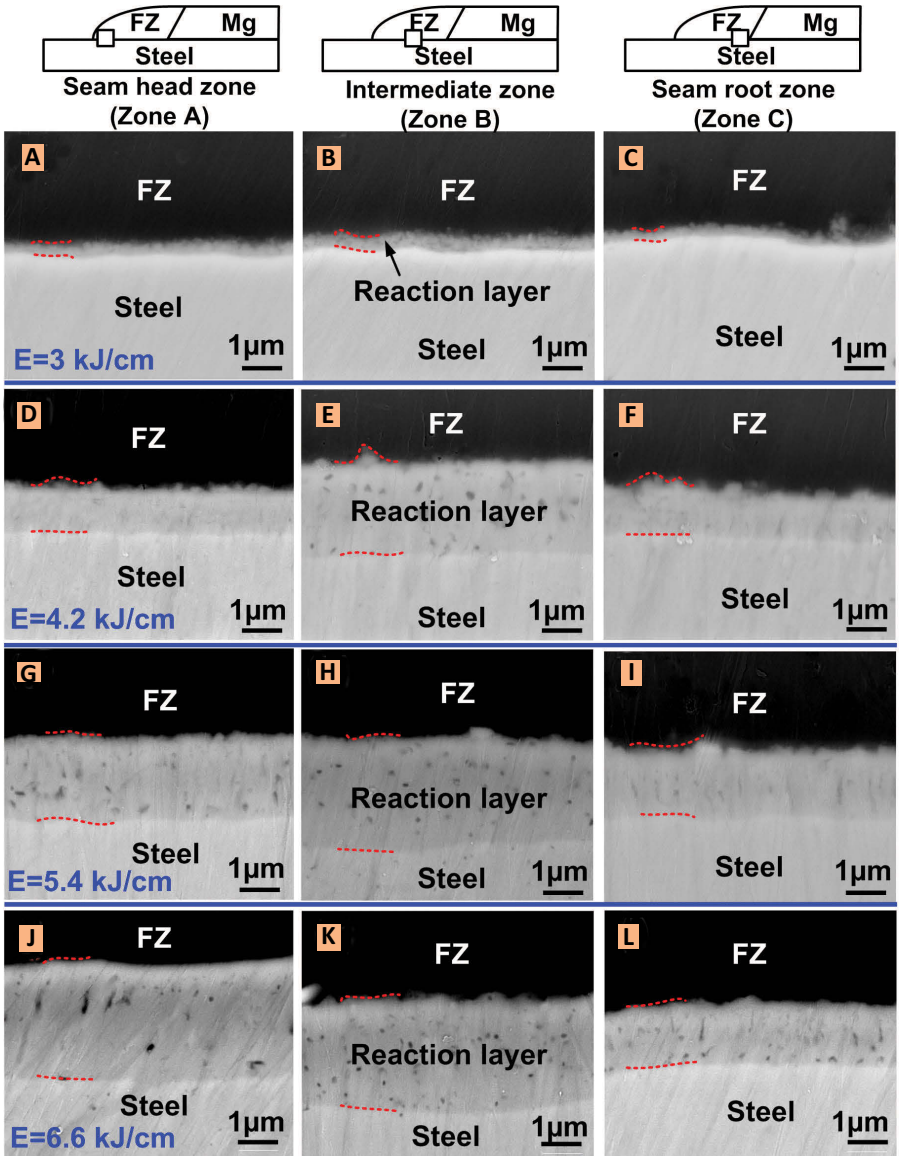

Fig. 4 — Steel-FZ interfacial microstructure at different heat inputs.

Table 3 — Laser Welding-Brazing Process Parameters Used in Current Study

Laser Power (W)	Travel Speed (m/min)	Wire Feeding Speed (m/min)	Heat Input (kJ/cm)
1000	0.2	0.6	3
1400	0.2	0.6	4.2
1800	0.2	0.6	5.4
2200	0.2	0.8	6.6

Table 4 — STEM-EDS Analysis Results of the Phases Formed at the Steel-FZ Interface (at.-%)

Phases	Mg	Al	Cr	Mn	Fe	Zn	Ni
I	60.01	29.20	0.50	0.39	2.50	7.37	—
II	6.86	61.90	2.82	17.48	9.95	0.96	—
III	1.08	23.32	12.96	6.63	55.89	0.01	0.08

ated using two modules in *FactSage*, i.e., Phase Diagram and Equilib modules. The Phase Diagram module of *FactSage* was used first to find all the possible formed phases in the Mg alloy fusion zone (FZ)-stainless steel system at different temperatures and compositions. The Equilib module was then used to identify the phases that were most likely to precipitate from the liquid at a specific temperature and composition among all the possible formed phases. This calculation was based on the principle of Gibbs free-energy minimization. The interfacial reaction products including the types of phases and their precipitation sequence were predicted after these two calculation procedure steps.

Results and Discussion

Appearances and Cross-Sectional Overviews

Figure 2 shows photographs of the laser brazed AZ31B Mg-stainless steel joints and typical cross-sectional overviews of the joints produced at different heat inputs. As shown in Fig. 2A, a lap joint with a rough surface was observed at the low heat input of 3 kJ/cm. Filler metal could not sufficiently wet the steel surface causing excessive deposition of the filler, since most of the energy from the laser beam was used to melt the filler metal. The steel substrate was poorly preheated due to insufficient heat input. With the increase of the heat input, the wetting of the filler on the steel was improved gradually. Smooth and uniform weld surfaces without obvious defects were evidenced, as shown in Fig. 2B, C. The excessive heat input caused severe evaporation of the filler metal resulting in an uneven bead appearance and porosity formation in the FZ as well as the steel-FZ interface, as shown in Fig. 2D.

Microstructural Analysis

Fusion Zone

Figure 3 shows a typical microstructure of the fusion zone on the magnesium side. Partial melting of the AZ31B base metal and mixing with the Mg-based filler metal produced the fusion zone. Four different microstructures were distinguished, i.e., base

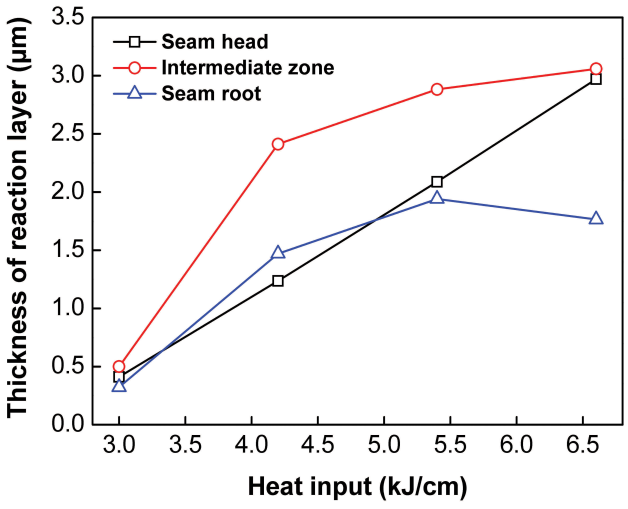

Fig. 5 — Reaction layer thickness vs. heat input.

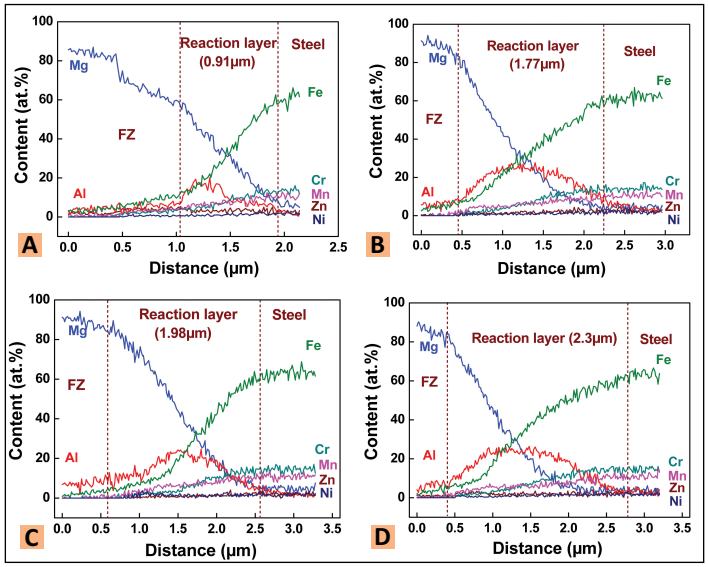

Fig. 6 — EDS line scans of Mg, Fe, Al, Zn, Mn, Cr, and Ni across the steel-FZ interface of the joint head at different heat inputs: A — 3 kJ/cm; B — 4.2 kJ/cm; C — 5.4 kJ/cm; D — 6.6 kJ/cm.

metal, heat-affected zone (HAZ), columnar crystal zone (CCZ), and equiaxed crystal zone (ECZ). Grain growth was found to take place in the HAZ toward the fusion zone, especially in the vicinity of the fusion zone. The precipitated β-$Mg_{17}Al_{12}$ phase was found distributed in the ECZ as indicated by arrows in Fig. 3. A more detailed microstructural analysis of the fusion zone can be found in our previous study (Ref. 32). The variation of microstructure in the fusion zone was found to affect the fracture mode, which will be discussed later.

Steel-FZ Interface

Figure 4 shows SEM images in different positions along the steel-FZ interface with variations in the heat input. A distinct interfacial layer was observed at the interface, indicating the occurrence of atomic diffusion and metallurgical bonding at the interface of Mg and Fe. A nonuniform, thick interfacial reaction layer was formed from the joint head to the root of the joint due to the temperature gradient resulting from the laser welding-brazing process (Ref. 24). The steel-FZ interfacial region was divided into three zones as marked in Fig. 4, i.e., joint head zone (Zone A), intermediate zone (Zone B), and joint root zone (Zone C). The reaction layer in all zones was found to exhibit a continuous morphology and its thickness at different heat inputs was measured and plotted in Fig. 5.

An ultrathin reaction layer (< 1 μm thick) was found at the low heat input of 3 kJ/cm. The thickness in the three zones was varied slightly due to insufficient reaction at such a low heat input. With the increase of the heat input, the thickness of the reaction layer grew slightly. For heat inputs of 4.2 and 5.4 kJ/cm, the thickness of the reaction layer at the intermediate zone was obviously larger than that at the joint head and the joint root. Note that the thickness of the reaction layer was always below 3 μm even with the excessive heat input of 6.6 kJ/cm. It suggested that metallurgical bonding at the interface was achieved while the thickness of reaction layer was controlled below 10 μm (Ref. 33), which was beneficial to the mechanical performance of the joints.

Concentration profiles of the main alloying elements across the interface between the fusion zone and steel were obtained using EDS line scanning analyses. Figure 6 shows the corresponding EDS line scan results. Cr and Mn increased gradually from the fusion zone side to the steel side. Zn and Ni, however, had no significant concentration variation across the interface. A high concentration of Al was found at the steel-FZ interface in all applied heat inputs. The results indicated that the Al atoms diffused from molten filler metal into the steel-FZ interface and then enriched at the interface, which induced the interfacial reaction.

The results in Figs. 4–6 confirmed the feasibility of joining Mg to steel through interatomic diffusion of alloying elements into each other at the interface. As shown in Fig. 4, in the case of the Mg-steel dissimilar metal combination, the reaction layer could not grow too thick even with applying excessive heat input, which was quite different compared with Al-steel or Al-Ti dissimilar metal joints (Refs. 20, 21, 24, 34). In those studies, it has been reported that the thickness of the Fe-Al and Al-Ti intermetallic reaction layers grows significantly with the increase of the heat input. The difference could be attributed to the amount of alloying elements involved in the interfacial reaction. In joining Al to steel or Al to Ti, the Al and Ti were the dominant alloying elements at the steel-FZ interface, which were sufficient for formation and growth of Fe_3Al and $TiAl_3$ phases. However, in our work, with 3 wt-% Al in the filler, Al content for diffusion-controlled growth of the reaction product was limited. As a result, the reaction was restricted causing the formation of the ultrathin reaction layer as shown in Fig. 4. At the same time, the fast heating and cooling rates experienced during the LWB process also limited the diffusion-controlled growth of

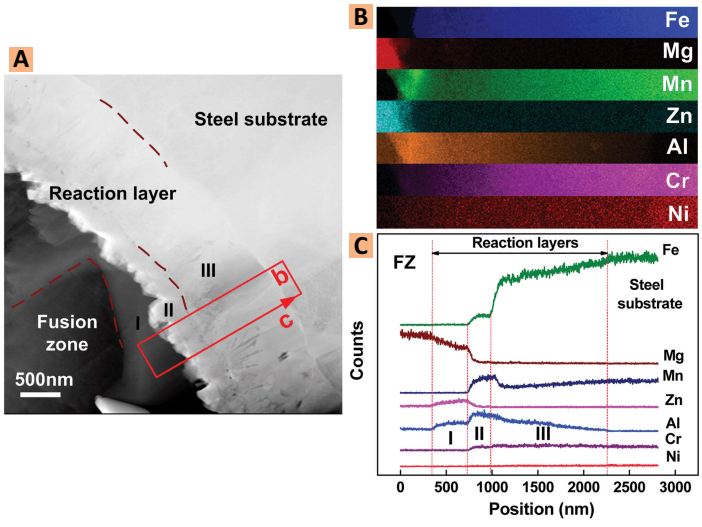

Fig. 7 — STEM image and STEM-EDS analyses results: A —STEM micrograph taken from the interface of the Mg-steel dissimilar joint; B — STEM-EDS mapping from the region indicated in A; C— STEM-EDS line scan results.

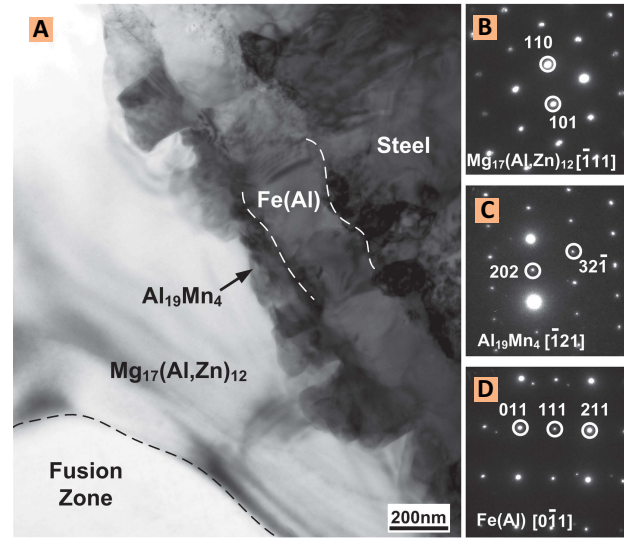

Fig. 8 — TEM investigation of the Mg-stainless steel interface: A — Bright field image taken from the interface; B–D — SADPs of the interfacial reaction phases.

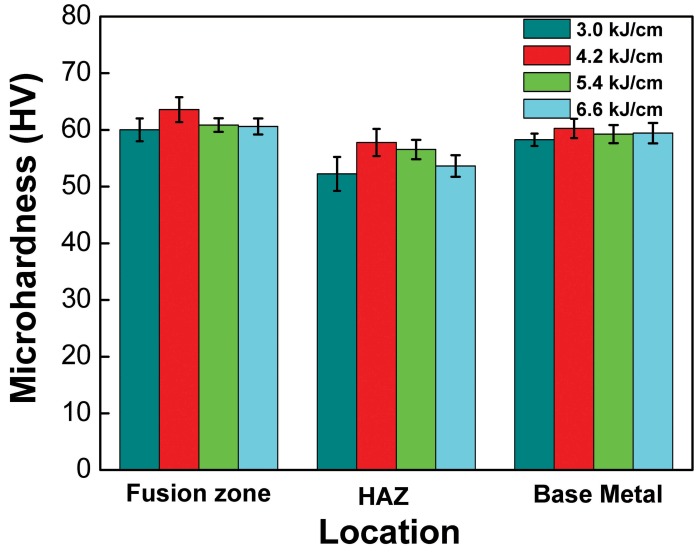

Fig. 9 — Hardness values in different locations of the Mg side.

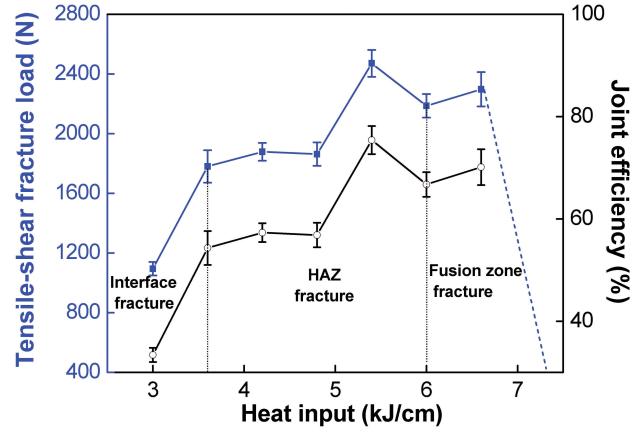

Fig. 10 — Tensile-shear fracture load and joint efficiency as a function of the heat input.

the interfacial layer.

Transmission electron microscope analysis was performed to identify the composition and structure of the reaction layer formed between the fusion zone and steel. Figure 7 shows a STEM micrograph taken from the steel-FZ interface made at 5.4 kJ/cm heat input. The newly formed interfacial reaction products were found as shown in Fig. 7A. Elemental distribution was investigated using STEM-EDS mapping analysis, and the results are shown in Fig. 7B. It can be seen that no mutual diffusion occurred between Mg and Fe since these elements are immiscible. In addition, high concentrations of Zn and Mn were found at the interface, which was not observed in the SEM line scan results. From the element mappings, it could also be observed that Al had the widest concentration at the interface. Concentration profiles of the alloying elements across the interface obtained from the STEM line scanning analysis are shown in Fig. 7C. It was clearly seen that alloying elements Al, Zn, and Mn concentrated at the interface at different regions. In region I, Al and Zn exhibited a continuous gradient. In region II, the concentration of Al continued to increase to a higher level. At the same time, a significant diffusion of Mn from the steel toward the interface was also noticed. In region III, the Al content decreased gradually, showing mutual diffusion of Al and Fe. In addition, it was also found that Al was involved in all interfacial reactions indicating that it acted as the dominant alloying element to bond immiscible Mg and Fe. The concentration of Cr and Ni had no enrichment in the interfacial regions.

Figure 8 shows a TEM micrograph with corresponding selected area

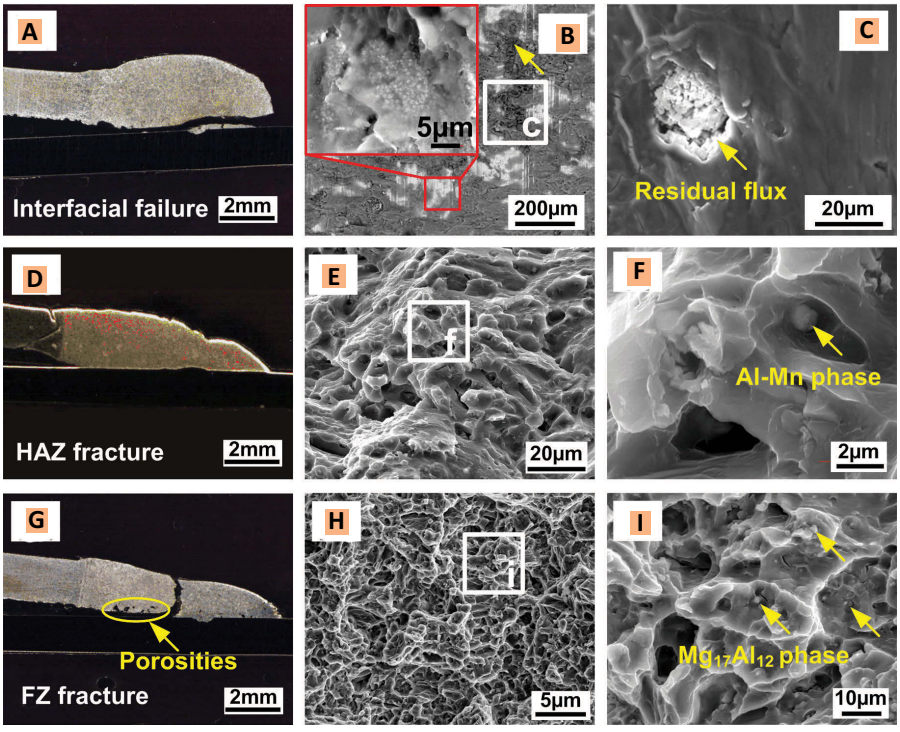

Fig. 11 — Fracture surface analysis of the Mg-stainless joints at different fracture modes: A, D, and G — Cross-sectional overviews showing different fracture modes; B, E, and H — SEM images of fracture surface of A, D, and G, respectively; C, F, and I — higher magnification of the square area indicated by C, F, and I, respectively.

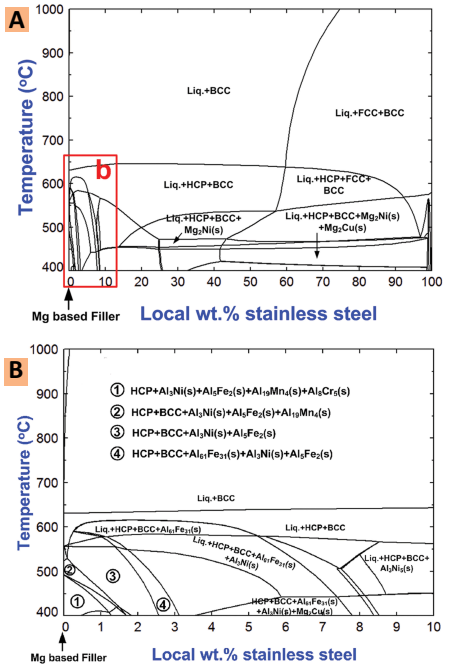

Fig. 12 — The calculated pseudo-binary phase diagram showing the phases that possibly form along the steel-FZ interface: A — The whole diagram; B — partial enlarged view of the diagram indicated by b in A.

diffraction pattern (SADP) taken from the interface of steel-FZ. The ultra-thin reaction layer was composed of three different nanoscale phases as shown in the bright field TEM image in Fig. 8A. The phase on the steel substrate was found to exhibit a uniform and continuous morphology followed by an irregular-shaped phase in the fusion zone.

The corresponding STEM-EDS analysis results are shown in Table 4. Combined with the indexed SADP results, shown in Fig. 8B–D, the phases from the fusion zone toward the steel were identified as $Mg_{17}(Al,Zn)_{12}$ IMC with body-centered-cubic (BCC) structure, $Al_{19}Mn_4$ with BCC structure, and Fe(Al) solid solution again with BCC crystal structure, respectively. Some of the Al atoms in the $Mg_{17}Al_{12}$ phase have been replaced by Zn atoms. This phase is a typical precipitate in the AZ series of Mg alloys and was produced in the fusion zone with a divorced eutectic structure, since the two eutectic phases (α-Mg + β-$Mg_{17}Al_{12}$) were separated from each other during the solidification. A similar observation has been reported in laser brazing of Mg to Al coated steel (Ref. 27). This phase was present occasionally at the interface. To be exact, the $Al_{19}Mn_4$ and Fe(Al) phases should be considered as the newly formed interfacial phases during LWB of Mg to stainless steel.

Mechanical Properties

Hardness Distribution

The hardness distribution values of the FZ, Mg HAZ, and the Mg base metal of the joints at different heat inputs are plotted in Fig. 9. The hardness of the HAZ was lower than that of the base metal due to HAZ softening as a result of grain coarsening and dissolution of strengthening precipitates induced by the thermal cycle during the LWB process (Refs. 35, 36). A slight increase in the hardness of the FZ, which was probably attributed to the higher volume fraction of the $Mg_{17}Al_{12}$ precipitates in the FZ (shown in Fig. 3), was also found.

Tensile-Shear Strength and Fracture Behavior

Figure 10 shows the tensile-shear fracture loads of the laser brazed AZ31B Mg-stainless steel joints at various heat inputs. It was evident that the heat input had a significant influence on the tensile-shear strength of the joints. The strength of the joint produced with the low heat input of 3 kJ/cm was quite low giving rise to interfacial failure. When the heat input increased to 4.2 kJ/cm, the joint fracture load was enhanced to 1878 N, and the calculated joint efficiency was 57.3% with respect to the fracture load of the Mg base metal. The fracture location was at the Mg HAZ indicating a strong steel-FZ interface. The strength varied slightly with further increase in the heat input. The fracture load reached the maximum value of 2471 N at the heat input of 5.4 kJ/cm, representing 75.4% joint efficiency relative to the Mg base metal.

Figure 11 shows the SEM micrographs of the fracture surfaces with different fracture behaviors. For the dissimilar Mg-steel joints with interfacial failure mode, the fracture surface of the steel side was observed using the backscattered electrons (BSE). Three different phases were identified at the fracture surface in

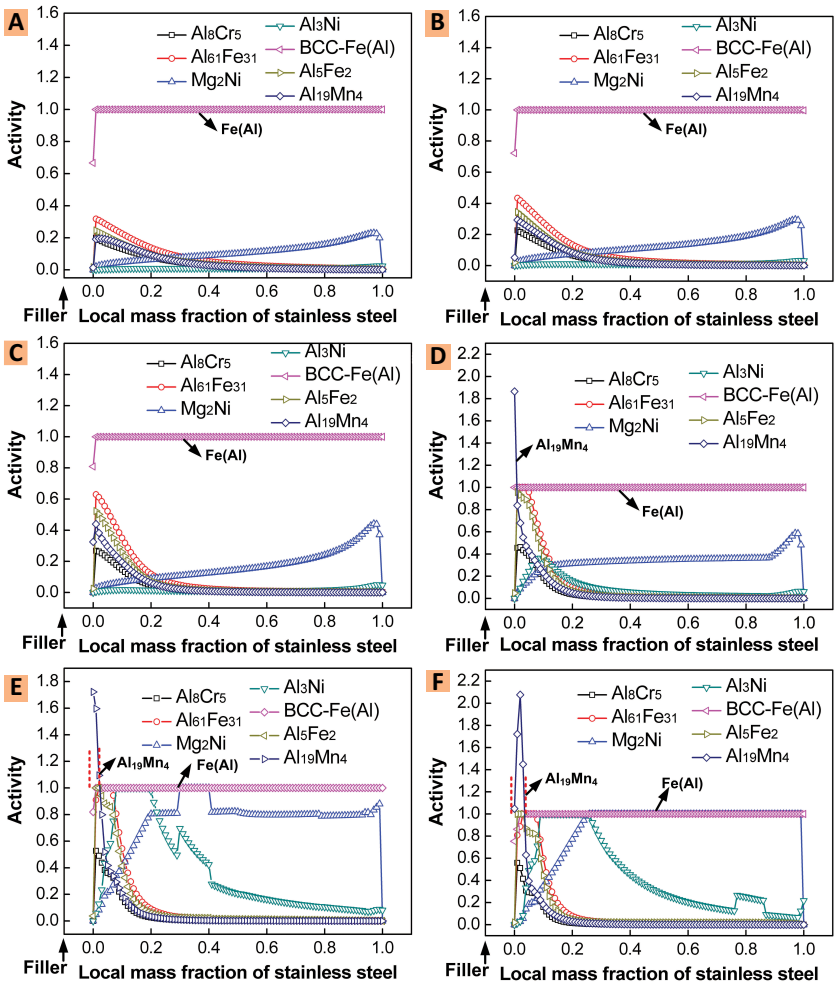

Fig. 13 — The activity-composition diagrams for possible phases formed at the AZ31 Mg-stainless steel interface at the following: A — 1100°C; B — 900°C; C — 700°C; D — 600°C; E — 500°C; F —400°C.

Fig. 11B. The gray matrix was residual Mg from the fusion zone attached to the steel side. A relatively bright phase was also observed distributed on the surface. A significant amount of particles were found at higher magnification, as shown in the inset of Fig. 11B. According to the EDS analysis results, this phase contained 18.9 at.-% Al and 81.1 at.-% Fe, representing Fe(Al) solid solution. In addition, a dark phase was also evidenced at the fracture surface as indicated by arrows. Energy-dispersive X-ray spectrometer examination of this phase confirmed that it contained 12.8 at.-% K and 13.8 at.-% Cl, suggesting that some of the flux was trapped in the interface during the process. This trapped flux in the steel-FZ interface degraded the mechanical strength of the joint significantly and resulted in an interfacial fracture. When fracture occurred in the Mg HAZ, the fracture morphology was characterized by dimples together with some cleavage-like flat facets, which were characteristics of a ductile fracture — Fig. 11E. The strengthening particles were observed at higher magnification as indicated by an arrow in Fig. 11F, which contained 58.4 at.-% Al and 41.6 at.-% Mn and were thus identified as Al-Mn phases by EDS analysis (Al_8Mn_5, typical of the AZ series of Mg alloys).

With the excessive heat input, the joint fractured in the fusion zone due to severe evaporation of the fusion zone, which caused a decrease in the joint width as well as porosity formation close to the steel-FZ interface. Porosities formed mainly close to the joint root zone, since the maximum temperature in this area was higher than that in the joint head zone, considering the position of the laser beam during the process. This explains why porosities were not observed from the intermediate zone to the joint head zone. During the tensile-shear test, the crack first initiated from the weak region, i.e., joint root zone, where the geometry of the joint created a high stress concentration area. Then, it propagated along the steel-FZ interface, where porosities existed. Finally, it deviated to the FZ, meaning the strength of the steel-FZ interface from the intermediate zone to the joint head zone was higher than that of the FZ. The corresponding FZ fracture surface was found to exhibit a dimple feature (see Fig. 11H, I). The difference here was the strengthening particles, which were found to be $Mg_{17}Al_{12}$ phase by EDS analysis.

Thermodynamic Analyses

Figure 12 shows the calculated pseudo-binary system between the Mg alloy (filler metal composition) and stainless steel composition over the temperature range of 400° to 1000°C using the Phase Diagram module of *FactSage*. This diagram was used to identify the phase(s) that might form along the steel-FZ interface at different temperatures during the laser welding-brazing process. These possible phases were Al_8Cr_5, $Al_{61}Fe_{31}$, Mg_2Ni, Al_3Ni, FeAl, Al_5Fe_2, and $Al_{19}Mn_4$. All the phases were found to be binary phases. In the next step, the most stable phase precipitated from the liquid at a specific temperature and composition should be identified, by finding which phase has the highest driving force to form from the fusion zone.

For a binary compound A_xB_y that forms from pure liquid components [*A*] and [*B*], the reaction process for formation of this compound from the filler metal-steel system in the laser welding-brazing process could be expressed as follows:

$$x[A] + y[B] \rightarrow AxBy\ (s) \qquad (1)$$

In order to predict what phases were stable under different conditions, the change of Gibbs free energy, ΔG, of the reaction shown in Equation 1 should be calculated. A negative ΔG

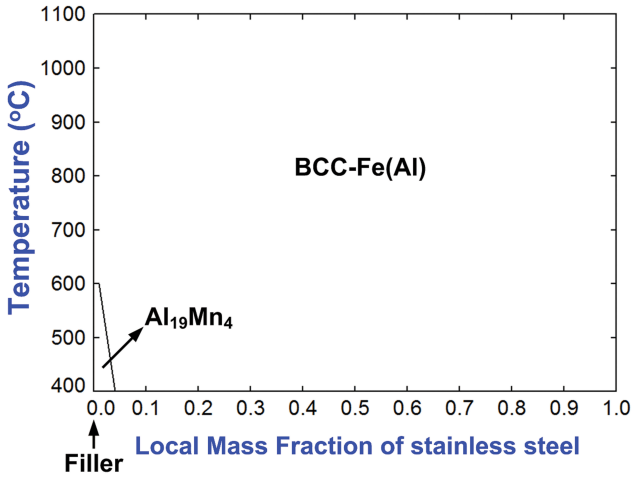

Fig. 14 — Phase stability map showing the most stable phases precipitated from the liquid at different temperatures and compositions during the laser welding-brazing process.

suggested that a process or chemical reaction would proceed spontaneously in the forward direction, whereas a positive ΔG indicated that the reaction would proceed spontaneously in reverse. The standard Gibbs free energy change of the reaction (ΔG°) indicated in Equation 1 can be determined using

$$\Delta G^{o}_{T,(A_xB_y)} = -RT\ln\frac{a(A_xB_y)}{a^x([A])a^y([B])} \quad (2)$$

where R is the universal gas constant, T is the absolute temperature (K), and a is the chemical activity of each phase (Ref. 37). For 1 mole of the elements, we have

$$\frac{x}{x+y}[A]+\frac{y}{x+y}[B]\rightarrow\frac{1}{x+y}A_xB_{y(s)} \quad (3)$$

Therefore,

$$\Delta G^{o}_{T,(A_{x/x+y}B_{y/X+y})} = -RT\ln\left(\frac{a(A_xB_y)}{a^x([A])a^y([B])}\right)^{\frac{1}{x+y}} \quad (4)$$

The chemical activity of [A] and [B] in the liquid state can be obtained for a given local temperature and composition. Thus, the chemical activity of A_xB_y(s) could be calculated once ΔG^{o}_{T} was obtained from the databases linked to the *FactSage* software. If $[a(AxBy)]^{1/x+y} > 1$, A_xB_y would form spontaneously. Note that a phase can precipitate in a form of a solid solution if $[a(AxBy)]^{1/x+y} = 1$ (Ref. 38). The greater the activity of the phase, the higher the driving force for formation of the phase. When there were many possible phases precipitated from the liquid at a specific temperature and composition, the phase with the maximum activity value would be the first precipitated phase and the most stable one. For 1 mole of the filler metal-steel system, the phase reaction and net change in free energy were as follows:

0.75 mole Al + 0.25 mole Ni will form 0.25 mole of Al_3Ni with a change of Gibbs free energy of

$$\Delta G^{o}_{T,(Al_{3/4}Ni_{1/4})} = -RT\ln\left(\frac{a(Al_3Ni)}{a^3([Al])a([Ni])}\right)^{\frac{1}{4}} \quad (5)$$

Similarly, 0.66 mole Mg + 0.33 mole Ni would form 0.33 mole of Mg_2Ni with a change of Gibbs free energy of

$$\Delta G^{o}_{T,(Mg_{2/3}Ni_{1/3})} = -RT\ln\left(\frac{a(Mg_2Ni)}{a^2([Mg])a([Ni])}\right)^{\frac{1}{3}} \quad (6)$$

0.826 mole Al + 0.174 mole Mn would form 0.043 mole of $Al_{19}Mn_4$ with a change of Gibbs free energy of

$$\Delta G^{o}_{T,(Al_{19/23}Mni_{4/23})} = -RT\ln\left(\frac{a(Al_{19}Mn_4)}{a^{19}([Al])a^4([Mn])}\right)^{\frac{1}{23}} \quad (7)$$

0.615 mole Al + 0.385 mole Cr would form 0.077 mole of Al_8Cr_5 with a change of Gibbs free energy of

$$\Delta G^{o}_{T,(Al_{8/13}Cr_{5/13})} = -RT\ln\left(\frac{a(Al_8Cr_5)}{a^8([Al])a^5(Cr)}\right)^{\frac{1}{13}} \quad (8)$$

0.714 mole Al + 0.286 mole Fe would form 0.143 mole of Al_5Fe_2 with a change of Gibbs free energy of

$$\Delta G^{o}_{T,(Al_{5/7}Fe_{2/7})} = -RT\ln\left(\frac{a(Al_5Fe_2)}{a^5([Al])a^2([Fe])}\right)^{\frac{1}{7}} \quad (9)$$

The component activities were calculated using the Equilib module of *FactSage* at different laser welding-brazing temperatures. Figure 13 shows the activity-composition diagrams for Al_8Cr_5, $Al_{61}Fe_{31}$, Mg_2Ni, Al_3Ni, FeAl, Al_5Fe_2, and $Al_{19}Mn_4$ from 1100° to 400°C. The composition in X axis should be considered as an approximated position between the liquid filler (x = 0) and an initial position on the filler-steel interface (x = 1). In the temperature range of 700° to 1100°C, Fe(Al) was predicted to be the first and only precipitated phase from the liquid. However, in the temperature range of 400°–600°C, $Al_{19}Mn_4$ was predicted to be the first precipitated phase from the liquid close to the filler. Then FeAl solid solution with BCC crystal structure formed in between the $Al_{19}Mn_4$ and steel.

Using this calculation procedure, a phase stability map was plotted in Fig. 14 to show the first precipitated phases from the liquid at different temperatures and compositions during the laser welding-brazing process. This phase stability map indicated that the BCC-Fe(Al) phase would possibly form over a large composition range from 0.04 to 100% of mass fraction of stainless steel. $Al_{19}Mn_4$ would form immediately adjacent to the filler when the temperature dropped below 600°C.

These calculation results have con-

firmed the formation of solid solution Fe(Al) on the steel surface followed by $Al_{19}Mn_4$ IMC. The calculation results were in good agreement with the TEM analyses results shown in Fig. 8.

Conclusions

1) Dissimilar AZ31B Mg alloy and 201 stainless steel sheets were joined successfully by a laser welding-brazing process using AZ31 Mg alloy welding wire. A uniform and visually acceptable joint was obtained with a relatively large process window.

2) An ultrathin layer of reaction product was formed at the interface of the Mg-stainless steel joint. Its thickness was varied in the range of 0.5–3 μm at different heat inputs, which was beneficial to the joint strength.

3) From TEM analyses, three nanoscale layers were identified along the Mg alloy-steel interface, i.e., $Mg_{17}(Al,Zn)_{12}$, $Al_{19}Mn_4$ and Fe(Al), from the fusion zone toward the steel side, respectively. Interdiffusion of alloying elements from base metals caused the formation of these layers and hence the metallurgical bonding between the fusion zone and steel occurred.

4) The tensile shear test indicated that joints produced at 5.4 kJ/cm heat input exhibited the highest mechanical resistance reaching 2472 N fracture load, representing a 75.4% joint efficiency relative to the Mg base metal. Tensile-shear tests showed three different fracture modes, which was closely related to the heat input. Insufficient heat input caused interfacial failure with some residual flux trapped in the interface. The sufficient heat input led to a fracture in the HAZ of the Mg base metal. The excessive heat input resulted in the fracture of the fusion zone.

5) A computational thermodynamic analysis was conducted to predict the early stage phase formation in AZ31 Mg alloy-stainless steel multi-elements alloy system during the laser welding-brazing process, confirming that the $Al_{19}Mn_4$ and Fe(Al) phases are the most stable phases that form along the filler metal-steel interface. The Fe(Al) phase formed over a large composition range, while the $Al_{19}Mn_4$ phase was predicted to form in a narrow compositional range.

Acknowledgments

This work is supported by a special foundation for Scientific and Technical Innovation, Harbin (Grant No. 2012RFLXG028). One of the authors (C. W. Tan) is grateful for the financial support provided by the China Scholarship Council for studying in the University of Waterloo, Canada.

References

1. Kulekci, M. K. 2007. Magnesium and its alloys applications in automotive industry. *The International Journal of Advanced Manufacturing Technology* 39: 851–865.

2. Mordike, B., and Ebert, T. 2001. Magnesium properties — applications — potential. *Materials Science and Engineering: A* 302: 37–45.

3. Liu, L. M., and Zhao, X. 2008. Study on the weld joint of Mg alloy and steel by laser-GTA hybrid welding. *Materials Characterization* 59: 1279–1284.

4. Liu, L., and Qi, X. 2009. Effects of copper addition on microstructure and strength of the hybrid laser-TIG welded joints between magnesium alloy and mild steel. *Journal of Materials Science* 44: 5725–5731.

5. Liu, L., and Qi, X. 2010. Strengthening effect of nickel and copper interlayers on hybrid laser-TIG welded joints between magnesium alloy and mild steel. *Materials & Design* 31: 3960–3963.

6. Liu, L., Xiao, L., Feng, J. C., Tian, Y. H., Zhou, S. Q., and Zhou, Y. 2010. The mechanisms of resistance spot welding of magnesium to steel. *Metallurgical and Materials Transactions A* 41: 2651–2661.

7. Qi, X., and Song, G. 2010. Interfacial structure of the joints between magnesium alloy and mild steel with nickel as interlayer by hybrid laser-TIG welding. *Materials & Design* 31: 605–609.

8. Qi, X.-D., and Liu, L.-M. 2010. Comparative study on characteristics of hybrid laser-TIG welded AZ61/Q235 lap joints with and without interlayers. *Journal of Materials Science* 45: 3912–3920.

9. Liu, L., Xiao, L., Feng, J., Li, L., Esmaeili, S., and Zhou, Y. 2011. Bonding of immiscible Mg and Fe via a nanoscale Fe_2Al_5 transition layer. *Scripta Materialia* 65: 982–985.

10. Santella, M., Brown, E., Pozuelo, M., Pan, T. Y., and Yang, J. M. 2012. Details of Mg-Zn reactions in AZ31 to galvanised mild steel ultrasonic spot welds. *Science and Technology of Welding and Joining* 17: 219–224.

11. Nasiri, A. M., Weckman, D. C., and Zhou, Y. 2013. Interfacial microstructure of diode laser brazed AZ31B magnesium to steel sheet using a nickel interlayer. *Welding Journal* 92: 1-s to 10-s.

12. Elthalabawy, W. M., and Khan, T. I. 2010. Microstructural development of diffusion-brazed austenitic stainless steel to magnesium alloy using a nickel interlayer. *Materials Characterization* 61: 703–712.

13. Elthalabawy, W. M., and Khan, T. I. 2010. Eutectic bonding of austenitic stainless steel 316L to magnesium alloy AZ31 using copper interlayer. *The International Journal of Advanced Manufacturing Technology* 55: 235–241.

14. Elthalabawy, W., and Khan, T. 2011. Liquid phase bonding of 316L stainless steel to AZ31 magnesium alloy. *Journal of Materials Science & Technology* 27: 22–28.

15. Jana, S., Hovanski, Y., and Grant, G. J. 2010. Friction stir lap welding of magnesium alloy to steel: A preliminary investigation. *Metallurgical and Materials Transactions A* 41: 3173–3182.

16. Wei, Y., Li, J., Xiong, J., Huang, F., and Zhang, F. 2012. Microstructures and mechanical properties of magnesium alloy and stainless steel weld-joint made by friction stir lap welding. *Materials & Design* 33: 111–114.

17. Wahba, M., and Katayama, S. 2012. Laser welding of AZ31B magnesium alloy to Zn-coated steel. *Materials & Design* 35: 701–706.

18. Schneider, C., Weinberger, T., Inoue, J., Koseki, T., and Enzinger, N. 2011. Characterisation of interface of steel/magnesium FSW. *Science and Technology of Welding and Joining* 16: 100–107.

19. Chen, Y. C., and Nakata, K. 2010. Effect of surface states of steel on microstructure and mechanical properties of lap joints of magnesium alloy and steel by friction stir welding. *Science and Technology of Welding and Joining* 15: 293–298.

20. Song, Z., Nakata, K., Wu, A., and Liao, J. 2013. Interfacial microstructure and mechanical property of Ti6Al4V/A6061 dissimilar joint by direct laser brazing without filler metal and groove. *Materials Science and Engineering: A* 560: 111–120.

21. Chen, S. H., Li, L. Q., and Chen, Y. B. 2010. Interfacial reaction mode and its influence on tensile strength in laser joining Al alloy to Ti alloy. *Materials Science and Technology* 26: 230–235.

22. Chen, S., Li, L., Chen, Y., and Huang, J. 2011. Joining mechanism of Ti/Al dissimilar alloys during laser welding-brazing process. *Journal of Alloys and Compounds* 509: 891–898.

23. Chen, S., Li, L., Chen, Y., Dai, J., and Huang, J. 2011. Improving interfacial reaction nonhomogeneity during laser welding-brazing aluminum to titanium.

Materials & Design 32: 4408–4416.

24. Dharmendra, C., Rao, K. P., Wilden, J., and Reich, S. 2011. Study on laser welding-brazing of zinc coated steel to aluminum alloy with a zinc based filler. *Materials Science and Engineering: A* 528: 1497–1503.

25. Miao, Y. G., Han, D. F., Yao, J. Z., and Li, F. 2010. Microstructure and interface characteristics of laser penetration brazed magnesium alloy and steel. *Science and Technology of Welding and Joining* 15: 97–103.

26. Miao, Y., Han, D., Yao, J., and Li, F. 2010. Effect of laser offsets on joint performance of laser penetration brazing for magnesium alloy and steel. *Materials & Design* 31: 3121–3126.

27. Nasiri, A. M., Li, L., Kim, S. H., Zhou, Y., Weckman, D. C., and Nguyen, T. C. 2011. Microstructure and properties of laser brazed magnesium to coated steel. *Welding Journal* 90: 211-s to 219-s.

28. Tan, C. W., Chen, Y. B., Li, L. Q., and Guo, W. 2013. Comparative study of microstructure and mechanical properties of laser welded-brazed Mg/steel joints with four different coating surfaces. *Science and Technology of Welding & Joining* 18: 466–472.

29. Li, L., Tan, C., Chen, Y., Guo, W., and Song, F. 2013. Comparative study on microstructure and mechanical properties of laser welded-brazed Mg/mild steel and Mg/stainless steel joints. *Materials & Design* 43: 59–65.

30. Li, L., Tan, C., Chen, Y., Guo, W., and Mei, C. 2013. CO_2 laser welding-brazing characteristics of dissimilar metals AZ31B Mg alloy to Zn coated dual phase steel with Mg based filler. *Journal of Materials Processing Technology* 213: 361–375.

31. Li, L., Tan, C., Chen, Y., Guo, W., and Hu, X. 2012. Influence of Zn coating on interfacial reactions and mechanical properties during laser welding-brazing of Mg to steel. *Metallurgical and Materials Transactions A* 43: 4740–4754.

32. Xu, W., Chen, D. L., Liu, L., Mori, H., and Zhou, Y. 2012. Microstructure and mechanical properties of weld-bonded and resistance spot welded magnesium-to-steel dissimilar joints. *Materials Science and Engineering: A* 537: 11–24.

33. Laukant, H., Wallmann, C., Müller, M., Korte, M., Stirn, B., Haldenwanger, H. G., and Glatzel, U. 2005. Fluxless laser beam joining of aluminium with zinc coated steel. *Science and Technology of Welding and Joining* 10: 219–226.

34. Peyre, P., Sierra, G., Deschaux-Beaume, F., Stuart, D., and Fras, G. 2007. Generation of aluminium-steel joints with laser-induced reactive wetting. *Materials Science and Engineering: A* 444: 327–338.

35. Gao, M., Tang, H.-G., Chen, X.-F., and Zeng, X.-Y. 2012. High power fiber laser arc hybrid welding of AZ31B magnesium alloy. *Materials & Design* 42: 46–54.

36. Cao, X., Jahazi, M., Immarigeon, J. P., and Wallace, W. 2006. A review of laser welding techniques for magnesium alloys. *Journal of Materials Processing Technology* 171: 188–204.

37. Nasiri, A. M., Chartrand, P., Weckman, D. C., and Zhou, N. Y. 2012. Thermochemical analysis of phases formed at the interface of a Mg alloy-Ni-plated steel joint during laser brazing. *Metallurgical and Materials Transactions A* 44: 1937–1946.

38. Gaskell, D. R. 2003. *Introduction to the Thermodynamics of Materials.* Taylor & Francis.

Correction:

In the *Welding Journal* Research Supplement paper titled "Influence of Fluid Convection on Weld Pool Formation in Laser Cladding" by Y.S. Lee et al., published in the August 2014 issue, the authors regretfully did not include acknowledgements. They would now like to thank Rolls-Royce Corp. for its funding support and for providing laser cladding samples in their work. They also wish to thank NSF-I/UCRC: Center for Integrative Materials Joining Science for Energy Applications and J. S.Bader for helpful suggestions and interest in their project.